Dopant structural distortions in high-temperature superconductors: an active or a passive role?

Daniel Haskel,[a]* Edward A. Stern,[b] Fatih Dogan[c] and Arnie R. Moodenbaugh[d]

[a]Experimental Facilities Division, Advanced Photon Source, Argonne National Laboratory, Argonne IL 60439, USA, [b]Department of Physics, University of Washington, Seattle, Washington 98195, USA, [c]Department of Materials Science and Engineering, University of Washington, Seattle, Washington 98195, USA, and [d]Materials Science Division, Brookhaven National Laboratory, Upton, New York 11973, USA. E-mail: haskel@aps.anl.gov

The parent compounds of high-temperature superconductors, such as $YBa_2Cu_3O_6$ and La_2CuO_4, are strongly interacting electron systems, rendering them insulators with Mott–Hubbard gaps of a few electronvolts. Charge carriers (holes) are introduced by chemical doping, causing an insulator–metal (IM) transition and, at low temperatures, superconductivity. The role of dopants is widely seen as limited to the introduction of holes into the CuO_2 planes (*i.e.* occupying electronic states derived from Cu $3d_{x^2-y^2}$ and O $2p_{x,y}$ atomic orbitals). Most theories of high-T_c superconductivity deal with pairing interactions between these planar holes. Local distortions around dopants are poorly understood, because of the experimental difficulty in obtaining such information, particularly at low doping. This has resulted in the neglect, in most theories, of the effect of such distortions on the chemical and electronic structure of high-T_c superconductors. Angular-resolved X-ray absorption fine structure (XAFS) spectroscopy on oriented samples is an ideal technique to elucidate the dopant distortions. Element specificity, together with a large orientation dependence of the XAFS signal in these layered structures, allows the local structure around dopants to be resolved. Results are presented here on (Sr, Ba) and Ni dopants, which substitute at the La and Cu sites, respectively, of insulating La_2CuO_4. The relevance of the measured local distortions for a complete understanding of the normal and superconducting properties of cuprates is discussed.

Keywords: high-temperature superconductors; dopants; lattice distortions.

1. Introduction

The coherence length of high-temperature superconductors, which is the length scale of the attractive interaction between carriers forming Cooper pairs, is ~10 Å. The understanding of local structural inhomogeneities on this length scale and the way they affect the local electronic structure is of great importance for a full understanding of this class of materials. In insulating La_2CuO_4, free carriers (holes) are introduced by chemical substitution of divalent (Sr^{2+}, Ba^{2+}) ions for trivalent La^{3+} ions in the La_2O_2 planes that separate CuO_2 planes. Once superconducting, at (Sr, Ba) concentrations of ~3–12 at.% (Radaelli *et al.*, 1994), Ni substitution for Cu in the CuO_2 planes rapidly reduces T_c, with superconductivity disappearing at $\lesssim 3$ at.% Ni (Cieplak *et al.*, 1992). These substitutions are random and therefore local distortions around dopants are randomly distributed. Diffraction techniques, which are only sensitive to periodic arrangements of atoms, cannot determine the dopant distortions. Structural techniques that measure all pair correlation functions in a certain region of real space, such as the pair distribution function (PDF) analysis of neutron scattering data (Billinge & Egami, 1993), are dominated by correlations involving the majority atoms, rendering the signal of interest (dopant–neighbor correlations) a few % of the total signal. The short-ranged sensitivity of XAFS, coupled with its element specificity and polarization dependence in layered structures, renders it an ideal technique for quantitative determination of the local distortions around dopants.

2. Experimental

The use of angular-resolved XAFS for these studies is a necessity. The local environment at the La site is too complicated to be resolved by powder XAFS, as the oxygen near-neighbor environment is composed of nine oxygen atoms at six different distances in the r = 2.3–3 Å region of real space (Radaelli *et al.*, 1994). The Cu local environment is simpler (distorted octahedron), but the planar Cu—O(1) distances dominate the powder XAFS as a result of their higher degeneracy (four distances) and stronger bonding, compared to the doubly degenerate Cu—O(2) distances along the c axis. However, since these layered structures are highly anisotropic, angular-resolved XAFS allows the independent determination of in-plane and out-of-plane subsets of the local atomic structure.

We used powders magnetically aligned along their c axis for these studies. The main advantage of this method over single-crystal methods is twofold: (i) control of the thickness of the sample, enabling transmission experiments at the absorption edges of concentrated elements (La, Cu), and (ii) control of the orientation of the c axis with respect to the surface of the sample for fluorescence experiments at the absorption edges of dilute elements (Ni, Sr). The latter allows the measurement of c- and ab-polarized fluorescence XAFS in identical geometries (see Fig. 1). A potential disadvantage is that c-axis-aligned powder is randomly oriented in the ab plane. However, the low-temperature orthorhombic (LTO) structural ground state of $La_{2-x}Sr_xCuO_4$ is twinned in the ab plane (Chen *et al.*, 1991), so XAFS in twinned single crystals also effectively averages over the a and b orientations. For the low-temperature tetragonal (LTT) phase of $La_{2-x}Ba_xCuO_4$, $a = b$ so the XAFS with $\hat{E} \parallel ab$ plane is the same in random ab powder and single crystals.

Further experimental details, including sample preparation, characterization, XAFS measurements and quality of data, can be found in previous reports (Haskel *et al.*, 1996, 1997, 1999, 2000).

3. Sr doping

We concentrate on the O(2) apical O atoms as they are the most affected by Sr substitution. We have previously reported evidence for the existence of a double-site distribution for the apical O atoms near Sr atoms in $La_{2-x}Sr_xCuO_4$ with $0.075 \leq x \leq 0.36$ (Haskel *et al.*, 1997, 1999). This distribution could be described as two Sr—O(2) distances ($r \simeq 2.25$ Å and $r \simeq 2.55$ Å), with relative weights changing from 37–63% at $x \simeq 0.075$ to 10–90% at $x \simeq 0.3$, the longer distance always dominating. These studies were performed on samples synthesized by the solid-state reaction method; *i.e.* starting from oxide powders. We have recently extended and repeated these measurements on samples prepared by a different method, *i.e.* the combustion technique, in which highly chemically homogeneous precursor powders are obtained by starting from ionic solutions of related nitrates. As shown here, these new samples did not show the double-site distribution in the Sr—O(2) apical distance observed previously, despite samples

from both families having similar values of T_c. It follows that this double-site distribution is not an essential ingredient in the mechanism of superconductivity.

The single Sr—O(2) apical distance found in the newly synthesized samples, however, agrees well with the weighted average of the two Sr—O(2) distances found previously (Haskel *et al.*, 1999), as shown in Fig. 2 for the samples with $x = 0.07$ and 0.15. Our measurement of the centroid of the Sr—O(2) apical distribution is therefore robust and independent of sample preparation conditions. We also show in Fig. 2 that repeated measurements at different synchrotron radiation facilities are within uncertainties of each other, as is a comparison between transmission and fluorescence measurements on a sample with $x = 0.04$.

The Sr—O(2) apical distance differs significantly from the La—O(2) distance (Fig. 2). As expected, the average La/Sr—O(2) distance measured by crystallography (Radaelli *et al.*, 1994) is recovered by an appropriate weighted average of local distances, shown in the lower panel of Fig. 2. The longer Sr—O(2) distance ($\sim$0.1 Å) is readily understood from the weaker attraction experienced by the negatively charged O(2) ion to a divalent Sr^{2+} ion, compared to that towards a trivalent La^{3+} ion. Fig. 2 also shows a change of slope, at about $x = 0.06$, in the doping dependence of the Sr—O(2) distance. This region is where the IM transition occurs in this system. Since the O(2) apical oxygen bridges Sr and Cu atoms (Haskel *et al.*, 1997), this change in slope is related to that observed by crystallography (reversed in sign), at $x \simeq 0.06$, for the x dependence of the Cu—O(2) distance (Radaelli *et al.*, 1994). The response of the Sr—O(2) distance and not of the La—O(2) distance to the delocalization of the doped holes at the IM transition implies that in the insulating side the doped holes are localized in the vicinity of the Sr ions.

Electronic structure calculations for La_2CuO_4 find that in this undoped compound the states at the Fermi level are predominantly derived from Cu $3d_{x^2-y^2}$ and O $2p_{x,y}$ atomic orbitals, with planar symmetry (Pickett, 1989; Grant & McMahan, 1991). In a molecular picture, the highest occupied molecular orbitals are antibonding combinations of these states (Khomskii & Neimark, 1991). Out-of-plane O $2p_z$ orbitals are consistently found to lie below the Fermi level (Pickett, 1989). The states at the Fermi level are the first to be populated by the doped holes.

The orbital character of doped holes can be found by orientation-dependent X-ray absorption near-edge structure (XANES) measurements, which precisely probe the local 'empty' density of states (DOS) with orbital angular momentum dictated by dipole selection rules. Such measurements at the O K edge and Cu L_3 edges (Chen *et al.*, 1992) found that doped holes predominantly reside on oxygen sites (O $2p$ states) with the ratio of out-of-plane *versus* in-plane orbital character, $p_z/p_{x,y}$, increasing with Sr doping. Although a crucial result, band theory could not explain it, as lowering the Fermi level with hole doping, together with the assumption of rigid band behavior, does not result in significant O $2p_z$ DOS at the Fermi level (Pickett, 1989). We believe that Fig. 2 holds the key to understanding the XANES observation: near an Sr^{2+} ion, the O(2) apical O $2p_z$ states are pushed to higher energy (less bound) as a result of (*a*) a lower Madelung potential because of the Sr^{2+} substitution for La^{3+}, and (*b*) the increased overlap between O $2p_z$ and Cu $3d_{3z^2-r^2}$ orbitals that results from the O(2) motion towards Cu, only near Sr. This local increase in energy of O $2p_z$ states towards the Fermi level results in them becoming partially populated by doped holes. The observation in Fig. 2 that the local Sr—O(2) distance gradually increases with x above the IM transition is consistent with the increase in the $p_z/p_{x,y}$ ratio, which decreases the negative charge on the apical O(2) nearby an Sr site. Additional non-rigid band behavior that could contribute to the increase in this ratio comes from the contraction in Cu—O(1) planar distance arising from electron removal (hole doping) from antibonding states derived from Cu and O(1) planar orbitals (Radaelli *et al.*, 1994). This increases the overlap of O $p_{x,y}$ and Cu $3d_{x^2-y^2}$ orbitals, shifting their spectral weight to higher energies.

Explaining the highly anisotropic normal-state transport properties of high-T_c superconductors has remained a challenge since the first measurements on single crystals (Nakamura & Uchida, 1993).

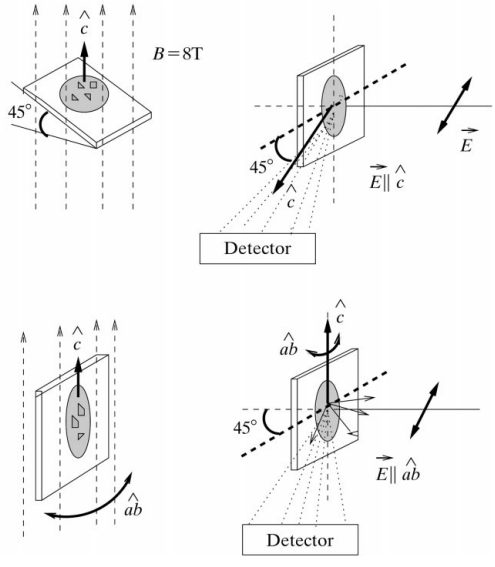

Figure 1
Special geometry used in the c-axis magnetic alignment of powders of $La_{1.85}Sr_{0.15}Cu_{1-y}Ni_yO_4$. This enabled the measurement of c and ab polarized fluorescence XAFS in identical geometries; *i.e.* $\hat{E}$ forming 45° with surface normal.

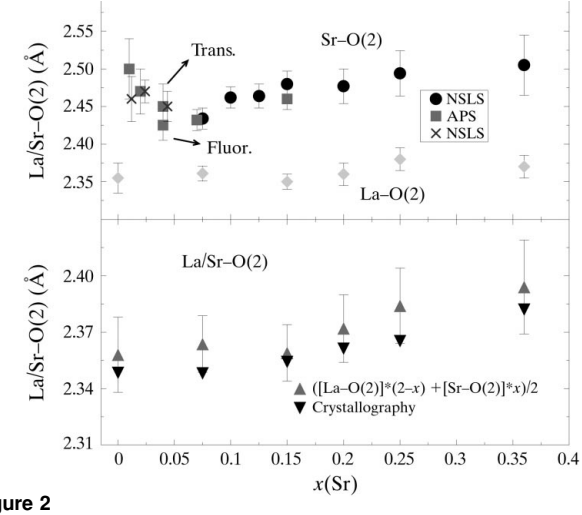

Figure 2
Top: local Sr—O(2) and La—O(2) apical distances as obtained from Sr and La K-edge measurements. Sr measurements were performed on samples prepared by solid-state reaction (circles) and a combustion technique (squares, crosses), and at different synchrotron facilities. For $x = 0.04$, results from both transmission and fluorescence are shown. Crosses are displaced for clarity. Circles are weighted averages (centroids) of the distribution of two Sr—O(2) distances found in our best fits of solid-state reaction samples (Haskel *et al.*, 1999). Bottom: weighted average of Sr—O(2) and La—O(2) distances and its comparison with the results of diffraction.

While the *ab* resistivity of $La_{2-x}Sr_xCuO_4$ is metallic above the IM transition, the *c*-axis resistivity remains semiconducting up to much higher values of doping (*e.g.* $\rho_c/\rho_{ab} \simeq 300$ at $x = 0.15$). This anisotropy, however, decreases with x and vanishes at $x \simeq 0.25$–0.3, where three-dimensional metallicity is observed. Bloch–Boltzmann transport theory using a local-density approximation (LDA) band structure (Allen *et al.*, 1987) predicts a nearly x-independent ρ_c/ρ_{ab} ratio of $\sim$30, in clear disagreement with experiment. Reasons for the inability of such calculations to explain the measured anisotropy probably include (*a*) an incorrect treatment of the anisotropy in the electron density, resulting in *c*-axis dispersions that are too large, and (*b*) neglect of the Sr—O(2) local distortion and related failure of the rigid-band approximation to result in significant O $2p_z$ orbital character at the Fermi level.

The increase in out-of-plane O $2p_z$ orbital character for the doped holes with x is the most likely explanation for the decrease in transport anisotropy. O $2p_z$ orbitals extend along the *c* axis and provide connectivity along it. Planar holes with O $2p_{x,y}$ orbital character extend in the CuO_2 planes along Cu—O(1) bonds, overlapping easily. O $2p_z$ holes at O(2) apical sites near Sr, however, have little overlap at low x. This explains why the IM transition at $x \simeq 0.06$ results in a two-dimensional metal with metallic CuO_2 planes. As x increases, the overlap between p_z holes near Sr sites increases. At $x \simeq 0.25$–0.3, where the *c* axis becomes metallic (Nakamura & Uchida, 1993), each Sr atom has, on average, at least one Sr neighbor in the La/Sr third shell. We note that O p_z holes will also have significant overlap in the *ab* direction. This might explain the unusual *c*-axis magneto-resistance of $La_{2-x}Sr_xCuO_4$, which is larger when the magnetic field is along *c*, in the same direction as the current, compared to that when the field is perpendicular to the current direction (Hussey *et al.*, 1998). This indicates that the carriers responsible for *c*-axis conduction spend a significant fraction of their time conducting in the *ab* direction, which is another indication of a very unusual normal state.

4. Ba doping

Although Sr and Ba doping in La_2CuO_4 are commonly thought of as equivalent, they are in fact very different. Ba doping brings about a different structural ground state in the superconductivity region of the phase diagram, the LTT phase, in which CuO_6 octahedra are rotated about ⟨110⟩-type axes, instead of the ⟨100⟩ tilts of the LTO phase (see Fig. 3). It is known that this new structure couples strongly with the hole carriers at $x \simeq 0.125$, with the strength of the coupling regulated by the magnitude of the tilt angle of CuO_6 octahedra (Pickett *et al.*, 1991). This coupling is manifested as an upturn of the resistivity below about 60 K, the temperature at which the LTT phase is stabilized, together with a strong T_c suppression (Moodenbaugh *et al.*, 1988). It has also been clear for some time that the LTT phase bears a large amount of intrinsic disorder, as evidenced in the very broad diffraction peaks and large thermal ellipsoids (Axe *et al.*, 1989), although a microscopic picture of the origin of such disorder has yet to emerge. Our measurements at all La, Cu and Ba sites of $La_{2-x}Ba_xCuO_4$ started shedding light on the nature and origin of such disorder (Haskel *et al.*, 2000).

We note that since the CuO_6 octahedra tilts are nearly rigid, first-shell Cu XAFS is insensitive to the tilt direction. However, La *K*-edge measurements with in-plane polarization ($E \perp c$) are very sensitive to the tilt direction and magnitude, as shown in Fig. 3 [the splitting of La—O(2) planar distances is a measure of the tilt angle]. We determined that the vast majority ($\gtrsim$95%) of local tilts are LTT-like, with a local tilt angle, averaged over all La sites, of $\langle\theta\rangle = 3.3\ (4)^\circ$, in good agreement with the 3.1 (3)° value found by diffraction (Haskel *et al.*, 2000). This average local tilt angle is determined from the first moment of the distribution of La—O(2) distances. The disorder in these distances, however, is a measure of the local fluctuations in tilt angle. That these fluctuations are above what is expected from thermal disorder considerations, is easily seen from the much larger σ^2 (by about a factor of two) obtained for distances involving oxygen atoms compared with those obtained for the same distances in the Sr-doped case (Haskel *et al.*, 2000). We directly determined the disorder in tilt angles by parameterizing the XAFS signals of the La—O(2)—Cu, Cu—O(2)—La/Ba and Cu—O(1)—Cu nearly collinear multiple-scattering (MS) paths in terms of their buckling angles (Fig. 4). The effective scattering amplitude of a nearly collinear MS path can be parameterized as $F_k(\beta) = F_k(\langle\beta\rangle)(\gamma_k + \zeta_k\beta^2)$ where $\langle\beta\rangle$ is the average buckling angle determined by diffraction techniques. Here γ_k and ζ_k are k-dependent coefficients obtained by fitting the β dependence of $F_k(\beta)/F_k(\langle\beta\rangle)$ for $\beta \lesssim 20^\circ$, using *FEFF*6 theory (Zabinsky *et al.*, 1995), separately for double-scattering and triple-scattering paths and for each value of k.

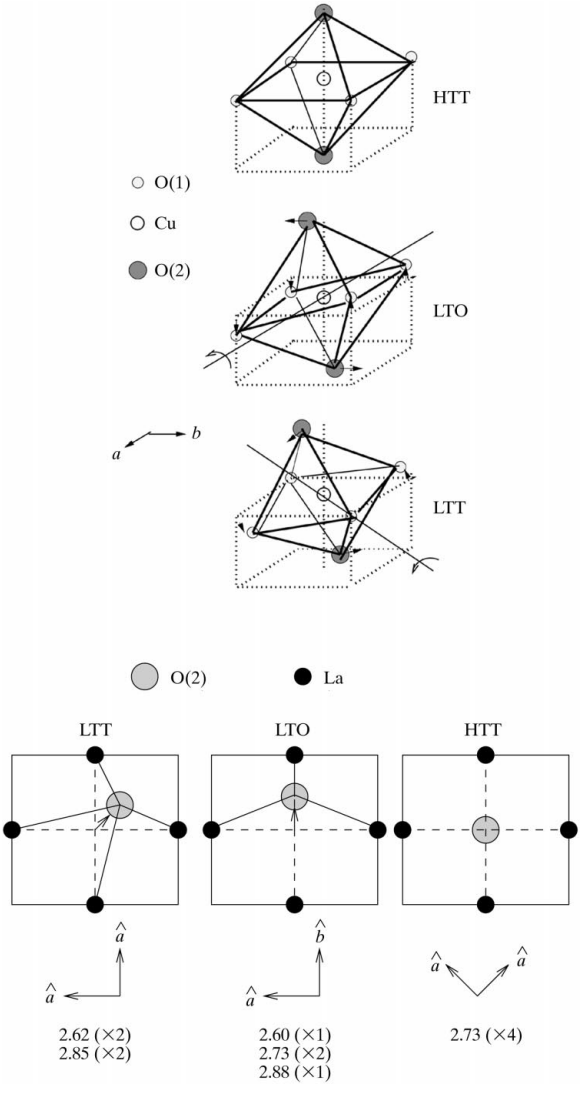

Figure 3
Top: CuO_6 octahedra tilt orientations for the different crystallographic phases of doped La_2CuO_4. Bottom: La—O(2) planar distances resulting from the tilts above; small correlated La displacements are not shown.

For a buckling angle that randomly deviates from its average value, $\beta = \langle\beta\rangle + \delta\beta$, XAFS can determine, through the effective scattering amplitude, $\langle\beta^2\rangle = \langle\beta\rangle^2 + \langle\delta\beta^2\rangle$, where an average over all absorbing atoms is performed. It follows that XAFS can determine the second moment of the local tilt-angle distribution, $\langle\delta\beta^2\rangle = \langle(\beta - \langle\beta\rangle)^2\rangle = \langle\beta^2\rangle - \langle\beta\rangle^2$, if the local first moment $\langle\beta\rangle$ is known. The case here is exceptional in that we could obtain this first moment directly from the La—O(2) distribution of distances. Our fits found a large amount of disorder in the magnitude of the local tilt angles, with r.m.s. variations of about twice the mean value; *i.e.* $\langle\delta\beta^2\rangle^{1/2} \simeq 2\langle\beta\rangle$ (Haskel *et al.*, 2000).

The large disorder in local tilt angle originates in the much larger ionic size of a Ba^{2+} ion (1.47 Å) compared with that of an La^{3+} ion (1.22 Å). This results in large local distortions around a Ba ion, which extend up to at least 5 Å from its lattice site (see Fig. 5). For a random solution, each Ba ion occupies a sphere of radius $R = r_s c^{-1/3} \simeq 5$ Å at $c \simeq 0.05$, where $(4/3)\pi r_s^3$ is the volume per La atom [$r_s \simeq (3.85/2)$ Å, 3.85 Å being an average La—La distance]. It follows that at $c \simeq 0.05$ ($x = 0.1$), where the new LTT phase appears (Axe *et al.*, 1989), the Ba distorted regions start overlapping with one another. It is this interaction that causes the development of the LTT phase in $La_{2-x}Ba_xCuO_4$. The large static disorder introduced with Ba doping is responsible for the lower T_c values and broader superconductivity transition curves compared with those in the Sr-doped system.

5. Ni doping

That we can learn about the nature of the superconducting state by destroying it, was nicely demonstrated in the scanning tunneling microscopy (STM) experiment of Pan *et al.* (2000) on Zn-doped $Bi_2Sr_2CaCu_2O_8$. Whereas no quasi-particle tunneling current is obtained at zero bias for most STM tip locations on the cleaved BiO surface (as a result of the gapped superconducting state), a zero-bias tunneling current is obtained when the STM tip is located precisely above a Zn dopant (two layers below the surface), indicating a 'metallic' state at the dopant site. By mapping the spatial extent of the Zn impurity state away from its lattice site in different directions, a *d*-wave-like image was obtained, with the impurity states extending further along the directions where the superconducting gap of a *d*-wave superconductor vanishes.

It is clear that the local structure around the dopant will influence the nature of the impurity states. It could also affect the tunneling cross section at a dopant site compared with that at a neighboring Cu site. Doping of Zn or Ni into the CuO_2 planes of superconducting cuprates has very similar effects: both contract the macroscopic *c* axis and suppress T_c. In $La_{1.85}Sr_{0.15}Cu_{1-y}Ni_yO_4$, superconductivity is destroyed at $y \simeq 0.03$ and an IM transition takes place at $y \simeq 0.05$ (Cieplak *et al.*, 1992).

Orientation-dependent XAFS measurements at the Ni *K* edge determined that the NiO_6 octahedra are locally contracted along the *c* axis, with Ni—O(2) apical distances shortened by as much as 0.16 Å, while the in-plane Ni—O(1) distances remain nearly unchanged (Haskel *et al.*, 2001). XANES measurements confirm the XAFS results, as the $4p_\pi$–$4p_\sigma$ splitting of ~3.0 eV (Fig. 6) corresponds well with the tetragonal distortion parameter $r_\parallel/r_\perp = 1.19$ measured by XAFS (Sahiner *et al.*, 1995).

The motion of the O(2) apical atom towards Ni induces a correlated displacement of La ions bonded to these O atoms, of about 0.06 Å, the measured contraction in the Ni—La distance [Ni—O(2)—La MS paths contribute at nearly the same distance]. The Sr atoms, however, are more weakly bound to the O(2) apical O atoms and do not follow their displacement toward Ni atoms. This is seen by comparing Sr and La *K*-edge measurements, in which a contraction of the La—O(2)—Cu/Ni distance is observed with increasing Ni content, while the Sr—O(2)—Cu/Ni distance remains nearly

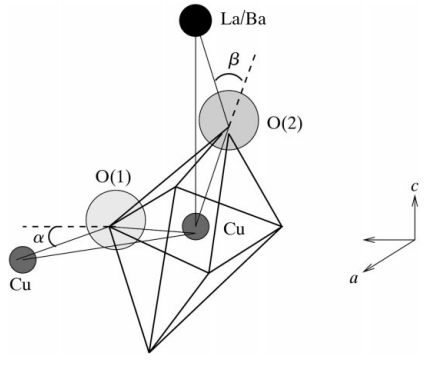

Figure 4
Schematic representation of CuO_6 octahedra tilts in the LTT phase, indicating the MS paths used in determining the fluctuations in the magnitude of tilt angle.

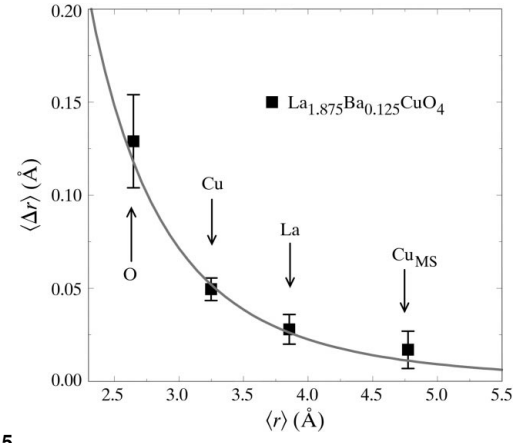

Figure 5
Angular-averaged radial atomic displacements from the lattice sites, $\langle\Delta r\rangle$, *versus* angular-averaged 'shell' distances, $\langle r\rangle$. The polarization dependence shows largely anisotropic distortions, but angular averages are shown for simplicity.

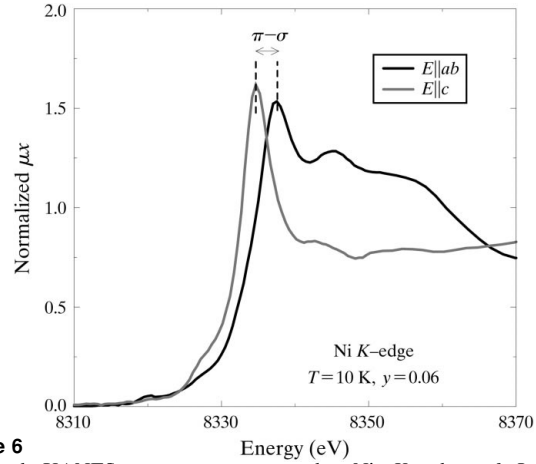

Figure 6
Polarized XANES measurements at the Ni *K* edge of $La_{1.85}Sr_{0.15}Cu_{0.94}Ni_{0.06}O_4$.

unchanged (Haskel *et al.*, 2001). It follows that the local *c* axis of Ni-doped $La_{2-x}Sr_xCuO_4$ is strongly modulated, with the largest variations occurring around the Ni sites.

As opposed to the case of a Cu^{2+} $3d^9$ ion, an Ni^{2+} $3d^8$ ion in its high-spin state is a non-Jahn–Teller ion. The energy advantage in having a spontaneous elongation of the octahedra disappears, since the occupation of $3d_{3z^2-r^2}$ and $3d_{x^2-y^2}$ orbitals is the same (Fig. 7). The measured non-Jahn–Teller state of Ni in $La_{2-x}Sr_xCuO_4$ is a direct proof of its high-spin state and rules out other electronic configurations, such as a low-spin state or a Ni^{3+} state that would have resulted from Ni trapping of doped holes. It should be noted that a tetragonal distortion remains, induced by the tetragonal crystal field of the lattice. Also, a fully relaxed non-Jahn–Teller ion would have exhibited an expansion of the planar Ni—O(1) distance, which is not observed. This testifies to the strength of the covalent bonding of the embedding CuO_2 planes, which opposes such relaxation. Zn doping is expected to exhibit a similar distortion, as a full-shell $3d^{10}$ Zn^{2+} ion is also non-Jahn–Teller. The very similar macroscopic *c*-axis contraction observed for both dopants supports this notion (Gaojie *et al.*, 1997).

Despite having a magnetic moment, Ni suppresses T_c at a similar rate to that found for non-magnetic Zn (Cieplak *et al.*, 1992). It is still unclear how the local distortion around Ni would contribute to such 'pair breaking', but it is reasonable to assume that doped holes will be scattered more strongly from such distorted centers. The spatial extent of a superconducting state cannot be confined to a region smaller than its coherence length (∼10 Å), as the resulting single-particle localization energy would be larger than the superconducting energy gap. It is possible that superconductivity is destroyed when the superconducting state is confined between such Ni centers, which at $y \simeq 0.03$ are separated by $2r_s c^{-1/2} \simeq 20$ Å ($2r_s \simeq 3.8$ Å).

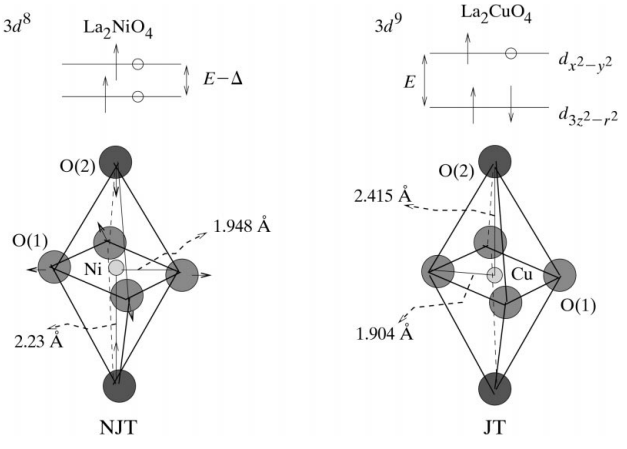

Figure 7
Schematics of the population of e_g molecular levels for octahedrally coordinated Cu $3d^9$ and Ni $3d^8$ ions in undoped $La_2(Cu,Ni)O_4$, along with their related octahedral environments. Although Ni^{2+} is a 'non-Jahn–Teller' ion, the degeneracy of e_g levels in La_2NiO_4 is lifted by the tetragonal crystal field of the layered structure. Sr doping in La_2CuO_4 contracts the Cu—O(1) distance and Ni doping in $La_{2-x}Sr_xCuO_4$ results in an Ni—O(2) distance similar to that in La_2NiO_4, but a planar Ni—O(1) distance similar to the Cu—O(1) distance in $La_{2-x}Sr_xCuO_4$.

6. Conclusions

New tools are becoming available that allow spectroscopy to be performed on high-T_c superconductors with atomic spatial resolution. These new techniques can only be fully exploited if a quantitative understanding of the local atomic environment is available. This is particularly important for doped compounds, in which the local structure is likely to differ from the structure determined by crystallography. Although no direct evidence is obtained from our measurements for a direct involvement of the dopant distortions in the mechanism of high-T_c superconductivity, they play a crucial role in determining the orbital character of doped holes, the anisotropy in normal-state transport, the stabilization of the LTT phase, and possibly contribute to 'pair breaking' when the dopants enter superconducting CuO_2 planes.

It is a pleasure to acknowledge Victor Polinger for fruitful discussions concerning the Jahn–Teller effect. Research was performed under auspices of DOE grant No. DE-FG03-98ER45681. DH was also partially supported by DOE contract No. W-31-109-Eng-38.

References

Allen, P. B., Pickett, W. E. & Krakauer, H. (1987). *Phys. Rev. B*, **36**, 3926–3929.
Axe, J. D., Moudden, A. H., Hohlwein, D., Cox, D. E., Mohanty, K. M., Moodenbaugh, A. R. & Xu, Y. (1989). *Phys. Rev. Lett.* **62**, 2751–2754.
Billinge, S. J. L. & Egami, T. (1993). *Phys. Rev. B*, **47**, 14386–14406.
Chen, C. H., Cheong, S. W., Werder, D. J., Cooper, A. S. & Rupp, L. W. (1991). *Physica C*, **175**, 301–309.
Chen, C. T., Tjeng, L. H., Kwo, J., Kao, H. L., Rudolf, P., Sette, F. & Fleming, R. M. (1992). *Phys. Rev. Lett.* **68**, 2543–2547.
Cieplak, M. Z., Guha, S., Kojima, H., Lindenfeld, P., Xiao, G., Xiao, J. Q. & Chien, C. L. (1992). *Phys. Rev. B*, **46** 5536–5547.
Gaojie, X., Zhiqiang, M., Mingliang, T., Yu, W. & Yuheng, Z. (1997). *J. Superconduct.* **10**, 13–18.
Grant, J. B. & McMahan, A. K. (1991). *Phys. Rev. Lett.*, **66**, 488–492.
Haskel, D., Stern, E. A., Hinks, D. G., Mitchell, A. W., Jorgensen, J. D. & Budnick, J. I. (1996). *Phys. Rev. Lett.* **76**, 439–442.
Haskel, D., Stern, E. A., Hinks, D. G., Mitchell, A. W. & Jorgensen, J. D. (1997). *Phys. Rev. B*, **56**, R521–R524.
Haskel, D., Polinger, V. & Stern, E. A. (1999). *AIP Conf. Proc.* **483**, 241–246.
Haskel, D., Stern, E. A., Dogan, F. & Moodenbaugh, A. R. (2000). *Phys. Rev. B*, **61**, 7055–7076.
Haskel, D., Stern, E. A., Polinger, V. & Dogan, F. (2001). *Phys. Rev. B.* Submitted.
Hussey, N. E., Cooper, J. R., Kodama, Y. & Nishihara, Y. (1998). *Phys. Rev. B*, **58**, R611–R614.
Khomskii, D. I. & Neimark, E. I. (1991). *Physica C*, **173**, 342–346.
Moodenbaugh, A. R., Xu, Y., Suenaga, M., Folkerts, T. J. & Shelton, R. N. (1988). *Phys. Rev. B*, **38**, 4596–4600.
Nakamura, Y. & Uchida, S. (1993). *Phys. Rev. B*, **47**, 8369–8372.
Pan, S. H., Hudson, E. W., Lang, K. M., Eisaki, H., Uchida, S. & Davis, J. C. (2000). *Nature (London)*, **403**, 746–750.
Pickett, W. E. (1989). *Rev. Mod. Phys.* **61**, 433–512.
Pickett, W. E., Cohen, R. E. & Krakauer, H. (1991). *Phys. Rev. Lett.* **67**, 228–231.
Radaelli, P. G., Hinks, D. G., Mitchell, A. W., Hunter, B. A. & Jorgensen, J. D. (1994). *Phys. Rev. B*, **49**, 4163–4175.
Sahiner, A., Croft, M., Guha, S., Perez, I., Zhang, Z., Greenblatt, M., Metcalf, P. A., Jahns, H. & Liang, G. (1995). *Phys. Rev. B*, **51**, 5879–5886.
Zabinsky, S., Rehr, J. J., Ankudinov, A., Albers, R. C. & Eller, M. J. (1995). *Phys. Rev. B*, **52**, 2995–3009.